Performance of the NREL S826 airfoil at low to moderate Reynolds numbers - A reference experiment for CFD models

Jan Bartl, Kristian F. Sagmo, Tania Bracchi, Lars Sætran

Department of Energy and Process Engineering, Norwegian University of Science and Technology, Kolbjørn Hejes veg 1B, N-7491 Trondheim, Norway

Abstract

Lift, drag and surface pressure measurements are performed on a wing section of the NREL S826 wind turbine airfoil at eight Reynolds numbers ranging from 0.5×10^5 to 6.0×10^5. Alongside with the measurements two types of Reynolds averaged Navier-Stokes (RANS) simulations are performed, one of which includes a laminar to turbulent transition model. The lift and drag characteristics are observed to be dominated by low Reynolds number effects for $Re < 0.7 \times 10^5$, related to the presence of laminar separation bubbles (LSBs) on the suction side of the profile. For $Re \geq 0.7 \times 10^5$ the airfoil's performance is rather independent of the Re-number for the present free stream turbulence intensities, while significantly higher peak lift is measured than in earlier experiments on the same airfoil. At high angles of attack, strong three-dimensional spanwise surface flow distribution reminiscent of a single stall cell is observed. The RANS simulations in a two-dimensional domain including the Langtry-Menter $\gamma - Re_\theta$ transition model accurately predict lift and drag coefficients as long as the flow is fairly attached. Further, the $\gamma - Re_\theta$ model simulations are observed to predict the location and average size of the LSBs in this region.

Keywords: NREL S826, airfoil performance, reference experiment, low Reynolds number, stall cells, laminar separation bubbles, transition modeling.

*Corresponding author
Email address: jan.bartl@ntnu.no ()

1. Introduction

With the advance of computational fluid dynamics (CFD) in all fields of engineering aerodynamics, well-defined experimental data sets for the validation of computational setups are needed. The objective of this combined experimental and computational study is two-fold.

The first objective is to provide experimentally obtained airfoil polars at low to medium Reynolds numbers for the NREL S826, which serve as important input data for Blade Element Momentum (BEM) or Actuator Line (ACL) simulations of wind turbine rotors. The BEM approach is the most commonly used method in the design process of wind turbine rotors, having the big advantage of a very fast simulation of the rotor's aerodynamic performance [1]. As an input, BEM simulations require aerodynamic polars for the Reynolds number range the blade elements are operating in. The NREL S826 airfoil was originally designed for mid-scale wind turbines at the National Renewable Energy Laboratory (NREL). A detailed description of the airfoils characteristics is given in [2]. Therein, the geometry is specified and the performance characteristics for chord length based Reynolds numbers from $Re_c = 1.0 \times 10^6$ to 3.0×10^6 are assessed. Since 2011, four blind test experiments on the performance and wake development behind model wind turbines of a rotor diameter of $D = 0.90\,m$ have been carried out at the Norwegian University of Science and Technology [3, 4, 5, 6]. The model turbines rotors were designed based on the NREL S826 airfoil, however, much smaller Reynolds numbers of the magnitude $Re_{c,tip} = 1.0 \times 10^5$ were prevailing for these model experiments. It was concluded that some of the uncertainty in the prediction of turbine performance and wake data could be subscribed to different sets of airfoil polars used in the simulations. Therefore, two experimental studies on the airfoils performance at low to moderate Reynolds numbers have been conducted in the wake of the blind test workshops. Sarmast et al. [7] and later Sarlak et al. [8] performed experiments on a two dimensional S826 wing section of the chord length c_L =0.10 m at Denmarks Technical University

(DTU). They observed abrupt separation effects at low angles of attack already at $Re_c < 1.0 \times 10^5$. Another experimental set of S826 airfoil data is available by Ostovan et al. [9] realized at the Middle East Technical University (METU) in Turkey. They measured lift and drag coefficients from $Re_c = 0.72 \times 10^5$ to $Re_c = 1.45 \times 10^5$ on a wing section of a chord length of c_L=0.20 m. No indications of abrupt separation effects at the lowest Reynolds numbers were observed in this experiment, although a much lower peak lift than in the DTU experiments was measured.

The measured lift and drag data are aimed to serve as input data for BEM and ACL simulations of small-scale wind turbines, such as the blind test experiments. In particular, the polars should give an accurate account of the airfoil's performance characteristics under the specific flow conditions achieved at the NTNU wind tunnel.

A related challenge for CFD simulation methods is to accurately predict the point of transition between the laminar and turbulent boundary layer on the blade surface. For the investigated low to moderate Reynolds numbers in this experiment the initial boundary layer on the airfoil surface develops typically laminar. The laminar boundary layer separates when exposed to a large adverse pressure gradient and forms a LSB. Further downstream, the laminar shear layer destabilizes and undergoes a transition to turbulent flow [10]. Due to a high momentum transport perpendicular to the airfoil surface the shear layer is able to re-attach. According to Kerho and Bragg [11] this happens as soon as turbulent mixing has eliminated the reverse near-surface flow. Hence, the second objective is that the present data shall serve as a reference experiment for state-of-the-art CFD modeling. The numerical computations reported here builds up on a previous study presented by Sagmo et al. [12], in which a initial experimental dataset was used for reference. The present study includes the final, repeated experimental dataset and also adds computations using the $\gamma - Re_\theta$ laminar to turbulent transitional model presented by Langtry and Menter [13]. An updated set of fully turbulent simulations using the Realizable $k - \epsilon$ turbulence model is included for direct comparison. Other numerical simulations of

the NREL S826 airfoil were performed by Sarlak et al. [8] as well as Cakmakcioglu et al. [14]. Cakmakcioglu et al. carried out simulations in a 2D and 3D domain using a Langtry-Menter ($\gamma - Re_\theta$) transition model as well as a Delayed Detached Eddy Simulation (DDES) in the stall region. As expected, they observed increased accuracy at stall with 3D simulations. At stall, DDES did not give improved results compared to 3D-transitional modeling, but was computationally more expensive. Sarlak et al. [8] performed three-dimensional Large Eddy Simulations on a S826 wing and compared them to DTU's experimental results. The LES simulations resulted in higher lift predictions compared to experimental results, especially at the onset of stall. They furthermore discussed hysteresis effects while changing the angle of attack as well as three dimensional flow effects at stall [15]. Early experiments related to the 3D flow effects on a rectangular plan-form wing beyond stall were conducted by Winkelmann and Barlow [16], as well as Weihs and Katz [17]. A more recent comprehensive study was conducted by Manolesos et al. [18] which combined experimental and computational investigations. Manolesos found inherently unstable stall cells on the wing's suction side (aspect ratio AR=2) at higher angles off attack and managed to reproduce experimental results computationally. Furthermore, the study indicated a strong interaction of the stall cell vortices with the trailing edge line vortices, which caused a inward deflection and consequently a strong spanwise variation of the force coefficients. In a continuation of this work, Manolesos and Voutsinas [19] also investigated the influence of Reynolds number, aspect ratio and angle of attack on the formation of stall cells.

The presented set of experimental data shall thus serve as a well-documented reference experiment for validation of CFD tools, offering a detailed database of the flow features around the NREL S826 airfoil. In this paper, we give an example on steady state RANS modeling of transitional effects such as laminar separation bubbles as well as three-dimensional flow effects at the onset of stall. The capability of predicting transitional effects by the Langtry-Menter $\gamma - Re_\theta$ transitional model is tested and the influence on the airfoil performance analyzed.

2. Experimental setup

2.1. Wind tunnel & inflow conditions

The experimental data of this study are measured in the closed-loop wind tunnel at NTNU in Trondheim. The rectangular test section of the wind tunnel is 2.71 m broad, 1.81 m high and 11.15 m long. The wind tunnel inlet speed is controlled by an inlet contraction, which is equipped with static pressure holes at the circumferences at two defined cross sections. The wind tunnel is driven by a $220kW$ fan located downstream of the test section being able to generate maximum wind speeds of up to $U_{max} \approx 25\,m/s$.

In order to assess the turbulence intensity level and integral turbulent length scale in the inflow, hot-wire measurements in the empty wind tunnel were performed at the wing position for all inflow Reynolds numbers. Table 1 shows the turbulence intensity levels measured in the empty tunnel for the whole Reynolds number range. Outside the wind tunnel boundary layers, the mean velocity in the empty tunnel was found to be uniform within 0.6% for all Reynolds numbers. The boundary layer thickness at wind tunnel walls is measured to be y_{BL}=0.220 m for a Reynolds number of $Re_c = 3.0 \times 10^5$ from the wind tunnel floor at the wing position.

2.2. Geometry and test rig setup

The NREL S826 airfoil was originally designed by Somers [2] at the National Renewable Energy Laboratory to be used at the blade tip of horizontal-axis wind turbines of a rotor diameter of $20-40m$. The primary objective was to obtain a maximum lift coefficient $C_L > 1.40$ at $Re = 1.0 \times 10^6$, low sensitivity to roughness and low profile drag. The airfoil was designed for high Reynold numbers $Re \geq 1.0 \times 10^6$, but was then utilized for Reynolds numbers one magnitude lower in NTNU's Blind test experiments. This discrepancy in Reynolds number then motivated the investigation of the airfoil's characteristics in transitional

Table 1: Turbulence Intensity levels (TI) and Integral turbulent length scales (L_{uu}) at the test rig location for all Reynolds numbers.

Re_c $[-]$	U_{ref} $[m/s]$	TI [%]	L_{uu} $[m]$
0.5×10^5	1.47	0.71	0.0078
0.7×10^5	2.36	0.70	0.0072
1.0×10^5	3.17	0.70	0.0066
2.0×10^5	6.82	0.44	0.0214
3.0×10^5	9.91	0.32	0.0575
4.0×10^5	14.32	0.30	0.0867
5.0×10^5	18.30	0.27	0.1276
6.0×10^5	22.27	0.26	0.2828

flow regimes.

The physical geometry of the airfoil for this experiment is CNC-milled from the synthetic polyurethane based board material called ebaboard 1200. Several layers of black gloss paint are thereafter laid on the raw material. A surface roughness measurement confirms a hydraulically smooth surface, i.e. the mean roughness depth of the surface is within the viscous sublayer and thus not affecting the boundary layer profile or skin friction [20].

The cross-section is based on the original NREL S826 profile coordinates. As it was not possible to produce an infinitely thin trailing edge, a trailing edge thickness of $d_{TE} = 2\,mm$ was defined, to which the produced profile is converging to. Figure 1 shows a comparison of the original profile as designed by NREL and the actually produced profile at NTNU. The actual surface coordinates of the model were measured by a high-resolution digitizing arm. Furthermore, the location of the 32 pressure taps on the wing surface at midspan are indicted in Figure 1. The S826 wing test rig is set up vertically in the test section and has a chord length of $c = 0.45\,m$ and a total height of $h_{total} = 1.78\,m$. The wing model blocks between $\sigma = 2.5\%$ at $\alpha = 0°$ and $\sigma_{max} = 8.3\%$ at $\alpha_{max} = 30°$ of the wind tunnel cross section. At peak lift, around $\alpha = 13°$, a blockage ratio of $\sigma = 3.7\%$ is calculated, which is below the critical blockage ratio of $\sigma = 10\%$ [21]. In Figure 2 the test rig is set up in the wind tunnel is shown. The wing

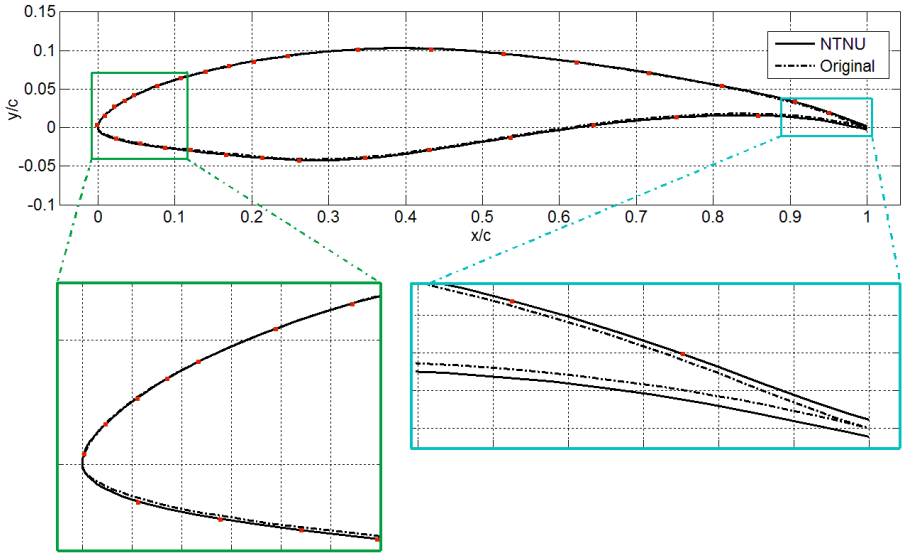

Figure 1: Comparison of the physically produced airfoil coordinates (NTNU) with the original design coordinates as designed by NREL (Original). The red points indicate the locations of the pressure taps around the circumference at mid-span.

consists of three main parts: the top dummy section, the central main section and the bottom dummy section. The main section is connected through rods in the inside of the wing to a 6-components force balance, which is located underneath the wind tunnel floor. Two holes of larger than the rods' diameter are drilled through the bottom dummy, in order to avoid a load transmission from the dummy part to the force balance. The bottom dummy is directly screwed into the rotating part of the wind tunnel floor through four small metal plates, without having any connection to the force balance located another 10 cm under it. Also the top dummy is directly connected to the rotating turntable part on the wind tunnel floor through two external rods visible in Figure 2 (a). These rods are placed approximately 100 cm from the wind surface to avoid any interaction with the flow around the wing. Additionally, there is a gap of about $2mm$ between main and dummy parts to avoid a force transmission between the two dummy parts and the main wing section. The dummy parts are designed

Table 2: Geometrical measures of the S826 wind test rig.

Airfoil chord length	$c_L = 0.45\,\mathrm{m}$
Total wing height	$h_{total} = 1.78\,\mathrm{m}$
Mid-section height	$h_{main} = 1.18\,\mathrm{m}$
Dummy height	$h_{dummy} = 0.30\,\mathrm{m}$
Gap between dummies and main part	$\Delta h_{gap} = 0.002\,\mathrm{m}$
Pressure taps location	$h_{taps} = 0.89\,\mathrm{m}$
Total wing aspect ratio	$AR = 3.95$

in order to cancel out interaction of the central wing section with the boundary layer flow near the test section's roof and floor.

At mid-span the wing is equipped with 32 pressure taps around the circumference as indicated in Figure 2. All important geometrical measures are summarized in Table 2.

2.3. Velocity, force and pressure measurements

A Pitot-static probe installed $x = 1\,m$ upstream of the test rig is used to obtain the free-stream velocity. The density of air is calculated from the temperature measured by a thermocouple inside the wind tunnel and the ambient pressure measured by a mercury manometer.

The mean and fluctuating surface pressure is measured by 32 pressure taps which are located around the wing's mid-span. As the taps are distributed in a straight line along the mid-span chord, a possible interference between the cannot be fully excluded. The taps are connected to a Electronically Scanned Pressure (ESP) transducer of the type DTC Initium mounted inside the wing as shown in Figure 2 (b). The sensors of the DTC Initium pressure scanner are made of piezo-resistive silicon which are sensitive to thermal variation, which is compensated for by digital temperature compensation in the system. The pressure scanners were periodically reset to minimize zero voltage drift. Thus, errors in pressure within $\pm 0.03\%$ of the full scale pressure range are ensured. Measurements are sampled for $t_{sample} = 60\,s$ with a sampling rate of $f_{Sample} = 500\,Hz$. From the measured surface pressure, distributions the normalized pressure, lift,

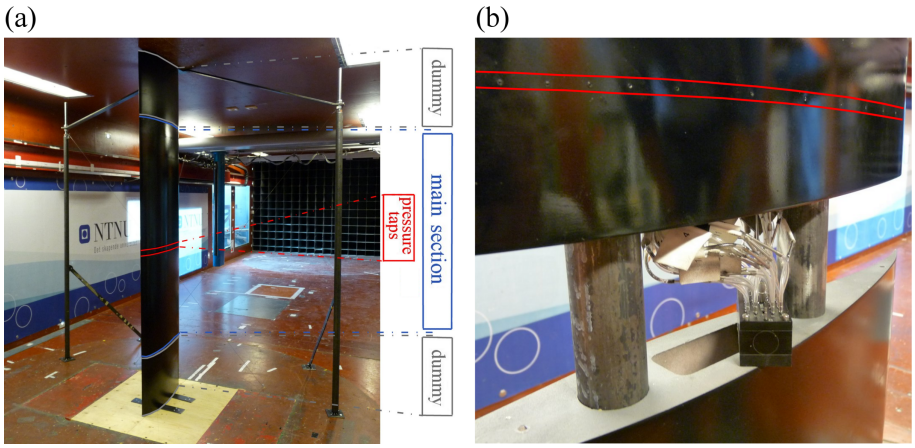

Figure 2: **(a)** The S826 test rig set up in wind tunnel test section. The rig consists of three parts: the main part in the center and two dummy parts at the wind tunnel floor and roof. **(b)** Detail: The pressure taps (marked between the red lines) and the 32-channel pressure transducer inside the opened wing.

drag were calculated by the following equations:

$$C_p = \frac{p}{\frac{1}{2}\,\rho\,U^2}, \tag{1}$$

$$C_{L,p} = \frac{f_L}{\frac{1}{2}\,\rho\,c_L\,U^2}, \tag{2}$$

$$C_{D,p} = \frac{f_D}{\frac{1}{2}\,\rho\,c_L\,U^2}. \tag{3}$$

Lift characteristics are measured by six-components force balance, on which the wing was mounted. Measurements were taken over a t_{sample} =60 s time interval and sampling rate of f_{Sample}=500 Hz. Automatic rotation of the force balance provided angle of attack in the range α=$-15°$ to $+30°$. Measured lift forces were normalized by the following equation:

$$C_{L,fb} = \frac{F_L}{\frac{1}{2}\,\rho\,c_L\,h\,U^2}. \tag{4}$$

A wake rake measuring total pressure was placed at $x = 0.7c$ distance downstream of trailing edge to measure pre-stall drag. A minor gradient was also

measured in the static pressure in the wake, but its contribution to the momentum loss in the wake core area was assessed to be insignificant. Twenty probes with a uniform spacing of $\Delta z = 10\,mm$ across the wake at the same height as the pressure taps. It has to be noted that the method of momentum deficit integration is more reliable than direct force measurements, but not considered to be reliable when the profile is stalled as the pressure probes are not capable of capturing the three-dimensional motions of the wake. Alternatively, the drag calculated from surface pressure integration or direct force measurement can be used for $\alpha > 15°$. For these high angles the pressure drag becomes dominant and is thus deemed to give a more accurate drag estimation. The static Pitot-probe upstream of the wing is used as reference pressure for the wake rake probes:

$$C_{D,wr} = \frac{F_D}{\frac{1}{2}\,\rho\, c_L\, h\, U^2}. \tag{5}$$

2.4. Statistical measurement uncertainties

Uncertainties in the lift- and drag measurement were calculated according to the methods described in [22]. Lift uncertainties were calculated from a systematic error estimate in velocity and force cell calibration as well as precision errors assessed from standard deviations in the single measurements. The resulting uncertainties were observed to rise in stalled conditions were plotted as errorbars in Figure 6. At its highest the total uncertainty in lift was calculated to be 3.5%. For the calculation of uncertainties in drag a minor decrease in static pressure along the wing tunnel had to be taken into account when assessing the wake momentum loss. Due to higher wake pressure fluctuations, larger uncertainties were computed for stalled angles of attack. Consequently, a significantly higher relative uncertainty of up to 20% was measured for the drag coefficient. The angle of attack could be adjusted with a measured accuracy of approximately $\Delta\alpha{=}\pm 0.25°$. The angle subtended by the mid chord line due to the trailing edge thickness of $2mm$ adds a $\pm 0.125°$ uncertainty in the angle of attack.

3. Computational methods

3.1. Numerical models

The implementation and calibration of $\gamma - Re_\theta$ transition model into Star-CCM+ is described in the paper by Malan et al. [23]. The Realizable $k-\epsilon$ turbulence model was run with a two-layer approach, which blends the two-equation model into the one equation model formulated by Wolfshtein [24] near the wall. The selected segregated flow solver was of second order, with an up-wind convection scheme implemented by a SIMPLE-like algorithm [25]. Moreover, the model settings assumed an isothermal, compressible and ideal gas.

3.2. Computational domain and grid

An illustration of the grids used is presented in Figure 3. The numerical study includes computational results on both a 2D and 3D grid. The 3D grid is essentially an extrusion of the 2D grid profile. An o-type mesh is used around the wing profile, with tangential wall normal extrusion layers extending 10 mm outwards to cover the boundary layer. A total of 42 to 62 wall layers were used. The bulk mesh was made up of trimmed, hexagonal cells, with multiple control volumes to contain cell growth. In order to facilitate the use of the $\gamma - Re_\theta$ transition model, all grids were designed to have wall $y^+ < 1$ over the airfoil surface. The grids were designed for a wall normal cell layer growth rate of 1.1, as it is recommended in [26]. The wing surface was modeled as hydraulically smooth, as justified by surface roughness measurements on the model used in the experiment. Both 2D and 3D grids are designed to match the exact dimensions of the NTNU wind tunnel test section used in the experiments. Simulations using the $\gamma - Re_\theta$ transition model requires a finer mesh resolution of the wing boundary layer compared to fully turbulent simulations. In order to facilitate this, all 3D simulations were run using a half domain, imposing symmetry conditions along the mid-span location. A summary of some key grid parameters is shown in Table 3. Another discrepancy worth pointing out was that the gap modeled between the airfoil measurement section and the wall dummies was exaggerated

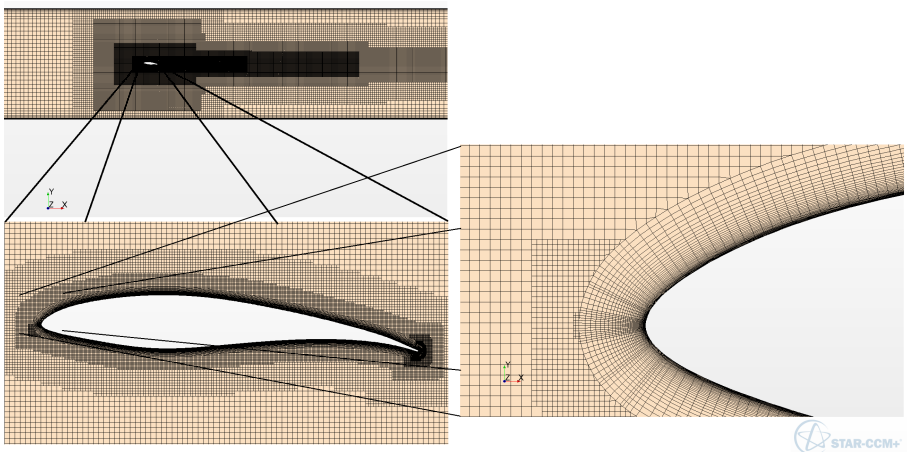

Figure 3: Illustration of grid cell distribution for mid-span x-y-plane used for most simulations, both 2D and 3D. Simulations for $\alpha = 12^{\circ}$ required a finer stream wise spacing of cells near the leading edge than shown here, due to a small laminar separation bubble.

to 4 mm in the simulations, so that a impact estimation could be made. Results comparing lift and drag coefficients computed from both continuous and split airfoil test section geometries are included in Table 6, Section 4.4.

3.3. Boundary conditions & wall treatment

The turbulence intensity (TI) and turbulence length scale (L_{uu}) are specified at the domain inlet in Star-CCM+. For this study the measured TI and L_{uu} values as listed in Table 1 were set at the inlet rather than the wing location. Due to the decay of turbulence a small error in the TI at the wing position is generated. However, for the present simulations the error generated was found to be small as shown in a sensitivity study included in Section 4.3, Table 5. The parameters turbulent kinetic energy k, turbulent dissipation rate ϵ and the specific turbulent dissipation rate ω are derived from TI and L_{uu} by the following relations:

$$k = \frac{3}{2}(TIv)^2, \tag{6}$$

$$\epsilon = \frac{C_{\mu}^{3/4} k^{3/2}}{L_{uu}}, \tag{7}$$

Table 3: Different surface cell sizes in percentage of the chord length. δ_{span} and δ_{chord} denote the span-wise and chord-wise cell spacing. $\delta_{w.cell}$ denotes the cell size in the wake behind the airfoil, stretching four chord lengths downstream. $\#_{tot}$ denotes the total cell count for each grid and $\triangle_{CPU}$ denotes the accumulated CPU time per iteration in seconds, referred to $\gamma - Re_\theta$ simulations. y^+_{max} denotes the maximum y^+ value of the first wall grid layer.

Grid	y^+_{max}	δ_{span}	δ_{chord}	$\delta_{w.cell}$	$\#_{tot}$	$\triangle_{CPU}$
2D coarse	0.595	-	(0.0129-0.35)%	(0.086-2.73)%	$6.88 \cdot 10^4$	1.17 s
2D medium	0.604	-	(0.0032-0.36)%	(0.043-1.39)%	$1.15 \cdot 10^5$	1.59 s
2D fine	0.614	-	(0.0020-0.17)%	(0.043-0.67)%	$3.04 \cdot 10^5$	4.82 s
3D medium	0.590	(0.087-0.35)%	(0.0013-0.35)%	(0.022-1.38)%	$5.33 \cdot 10^7$	1160 s

$$\omega = \frac{\sqrt{k}}{L_{uu}(\beta^*)^{1/4}}. \tag{8}$$

Here, v is the turbulent velocity scale (set to $\approx$3.17 ms^{-1} for $Re = 1.0\times10^5$), and C_μ and β^* are model coefficients. A dynamic pressure outlet of one atmosphere was set on the rear wall boundary. A previous investigation of the sensitivity of the downstream position of the pressure outlet using 2D simulations showed negligible effect on the overall drag and lift coefficients [12].

All the present simulations were shown to have wall y^+ <1, both for 2D and 3D. This induced a wall treatment similar to a low y^+ treatment. The low wall y^+ treatment in STARCCM+ makes no explicit modeling assumptions, and sets the the velocity distribution in the viscous sub-layer as $u^+_{laminar} = y^+$ [25]. The velocity distribution in the logarithmic layer is set to

$$u^+_{turbulent} = \frac{1}{\kappa} ln(Ey^+), \tag{9}$$

in which the von Karman constant is set to $\kappa = 0.42$, while E is set to the default constant $E = 0.9$. The definition of the dimensionless u^+ and y^+ stems from the usual *law of the wall* [27].

3.4. Iterative errors and grid discretization error estimation

All 2D simulations were run until a flat-lining of normalized model residuals below 10^{-5} was displayed. 3D simulations were generally observed to converge

Table 4: Gradual grid refinement computed in the 2D $\gamma - Re_\theta$ simulations. E_f represents the relative error compared to the fine grid solution. GCI_m denotes the medium grid-convergence index, relative to the fine grid solution values.

	$\alpha = 4°$				$\alpha = 8°$			
Grid	C_D	C_L	E_{f,C_D}	E_{f,C_L}	C_D	C_L	E_{f,C_D}	E_{f,C_L}
coarse	0.0240	0.953	0.53%	-0.79%	0.0322	1.307	4.20%	-1.44%
medium	0.0234	0.960	-2.04%	-0.01%	0.0305	1.325	-1.20%	-0.14%
fine	0.0239	0.960	-	-	0.0309	1.327	-	-
GCI_m[%]	3.27	0.02	-	-	1.93	0.23	-	-

with slightly higher orders of 10^{-3} in normalized residuals. As a first estimate for an iterative error, results were compared to values obtained at a large number of excessive iterations. The relative differences were usually well below 1% for the 3D simulations and lower than 0.001% for the 2D simulations. An exception for the 3D simulations was found for the prediction of drag coefficients at $\alpha = 10°$ and 12°, where the solution value varied with as much as 5% over the course of 2000 iterative steps. To give some estimate on the numerical discretization errors the procedure presented in the paper by Celik et al. [28] was followed. The method for reporting the so-called grid convergence indicator (CGI) is based on Richardson Extrapolation for discretization error estimation and also introduces a safety factor F_s. The mesh dependency study was conducted using 2D grids with three steps of varying resolution. These are referred to as the coarse, medium and fine grids. For $\alpha = 0°$, 4°, and 8° a slightly less refined wing surface mesh was used compared to the simulations at $\alpha = 12°$. This was due to a small leading edge separation bubble being predicted at $\alpha = 12°$, which required additional curvature refinement and wall normal cell layers to be properly resolved. In an effort to ensure that results converge for all setups, the stream wise grid spacing over the airfoil was not allowed to exceed a certain limit. Failing to resolve the laminar separation bubbles would result in simulations not properly converging. This restraint in grid coarsening for the airfoil boundary layer meant that, for instance, a base cell size doubling would

not necessarily lead to a 1/4 times reduction in total cell count. See Table 4 for a presentation of force coefficient results for different grid sizes using the Menter SST $k-\omega\ \gamma-Re_\theta$ model. Not all target values showed asymptotic behavior and due to small relative differences between the grid solutions a good estimate for the observed numerical order could not be computed. Instead, an assumed numerical order p=2 was chosen while the presented medium grid-convergence index was computed relative to the fine grid solution with a safety factor of $F_s = 1.25$ as recommended by Roache [29].

4. Results

In this section lift, drag and surface pressure distributions are presented. First, the experimental results for the lift and drag coefficients are given for all eight Reynolds numbers. Thereafter, the simulation results of three different simulation setups are compared to the experimental results. All pressure distributions are evaluated at mid-span. Special attention is given to transitional effects at selected angles of attack and the capability of the implemented transition models to capture these effects. Furthermore, three-dimensional flow effects at the onset of stall are investigated in detail.

4.1. Experimental results

The lift and drag coefficients of the NREL S826 wing were measured at eight different Reynolds numbers ranging from 0.5×10^5 to 6.0×10^5. The lift coefficients are obtained by direct force measurement on the mid-wing section, which was connected to the six-component force balance. The drag coefficients were calculated from the momentum loss measured in the wake behind the wing at mid-span. Figure 4 (a) shows the experimental lift results for all investigated Reynolds numbers. It should be noted that the inflow turbulence intensity and length scales vary according to the values given in Table 1. It is observed that the Reynolds number has a minor influence on the lift coefficient and drag coefficients for $Re \geq 0.7 \times 10^5$. The average lift curve slope in the linear lift region

between α =-8° − 10° is about 0.1 units C_L per degree. The maximum lift coefficient is found around $\alpha \approx 13°$, with a peak value of $C_{L,max} = 1.56$. Smaller deviations in lift are found for $\alpha < 7°$ for the lower Reynolds numbers 0.7 and 1.0×10^5, while the deviations are very small with α approaching $C_{L,max}$. In the deep-stall region for $\alpha > 15°$ the differences between the Reynolds numbers are observed to be slightly bigger again, indicating a somewhat later full flow separation with increasing Reynolds numbers. As an example, the lift coefficients range between $C_{L,20°,Re70k} = 1.17$ and $C_{L,20°,Re400k} = 1.30$ at $\alpha = 20°$. The lift characteristics measured at $Re = 0.5 \times 10^5$, however, are observed to be significantly different. For positive angles of attack between $\alpha = 2°$ and 8°, the lift curve collapses intermediately before reaching a lift level similar to that observed for higher Reynolds numbers at α $8°to10°$. For $\alpha \geq 11°$ an almost linear drop in lift is observed, resulting in considerably lower lift coefficient values compared to those measured for higher Reynolds numbers. A further subsequent drop in lift at $\alpha \approx 15°$ indicates a complex flow over the wing at $Re = 0.5 \times 10^5$.

The drag results are presented in Figure 4 (b) for the entire Reynolds number range. Full lines indicate the drag results measured from a momentum loss integration in the wake at mid-span, which is considered to be accurate for non-stalled flow conditions. At the onset of stall at $\alpha = 13°$ and beyond, drag results from direct force measurements as indicated by dashed lines, are deemed to give a more accurate drag estimation. In the pre-stall region measurement results for $Re > 1.0 \times 10^5$ are well aligned. However, the drag coefficients are in general observed to further decrease with increasing Reynolds number. A minimum in drag is found at $\alpha = 0°$ for all Reynolds numbers. Measurements for Reynolds numbers $Re \leq 1.0 \times 10^5$ result in a larger drag for the whole pre-stall region. At $\alpha = 0°$, for instance, the drag coefficients for $Re = 0.5 \times 10^5$ is measured to be $C_{D,0°,Re50k} = 0.0236$, while it is almost 50 % smaller for $Re = 2.0 \times 10^5$ only amounting $C_{D,0°,Re200k} = 0.0125$ respectively. As α approaches 14° the portion of separated flow on the upper airfoil surface increases, making the drag coefficient rise significantly for all Reynolds numbers. As previously observed

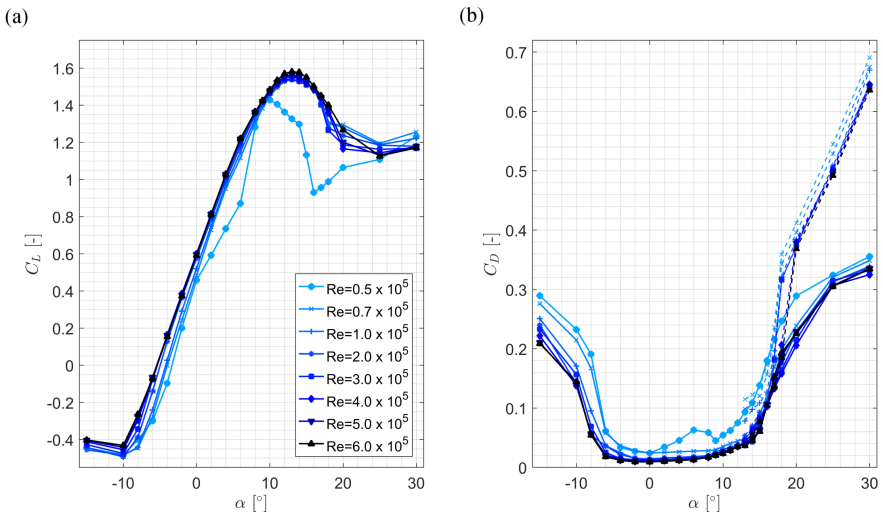

Figure 4: **(a)** Lift and **(b)** drag coefficients measured from $Re = 0.5 \times 10^5$ to $Re = 6.0 \times 10^5$. Lift coefficient results shown are obtained from direct force measurements in the wake. Drag coefficient results are calculated from the momentum loss in the wake at mid-span (full lines) and direct force measurements (dashed lines).

for the lift characteristics, also the drag coefficients for $Re = 0.5 \times 10^5$ show a different trend. A local rise in drag is already observed between $\alpha = 2°$ and 8°, corresponding to a local collapse in lift. At this low Reynolds number local re-circulation zones are suspected to cause a lift decrease and drag increase at certain angles of attack, which will be analyzed in more detail in the following sections. In Figure 5 the mean surface pressure distributions at mid-span at $\alpha =$ 0, 4, 8 and 12° are presented for a range of different Reynolds numbers. Due to a very high uncertainty in the results of $Re = 0.5 \times 10^5$, this Reynolds number is not plotted. Note that surface pressure distributions for $Re = 1.0 \times 10^5$ are included in Figure 7 and hence omitted in Figure 5 for clarity. For $Re = 0.7 \times 10^5$ substantial deviations are observed compared to higher Reynolds numbers. At all angels of attack the extent of laminar separation bubbles is considerably larger in this low Reynolds number regime. For example at α=4° the separation bubble occurs at both pressure and suction side. For $Re \geq 2.0 \times 10^5$ the

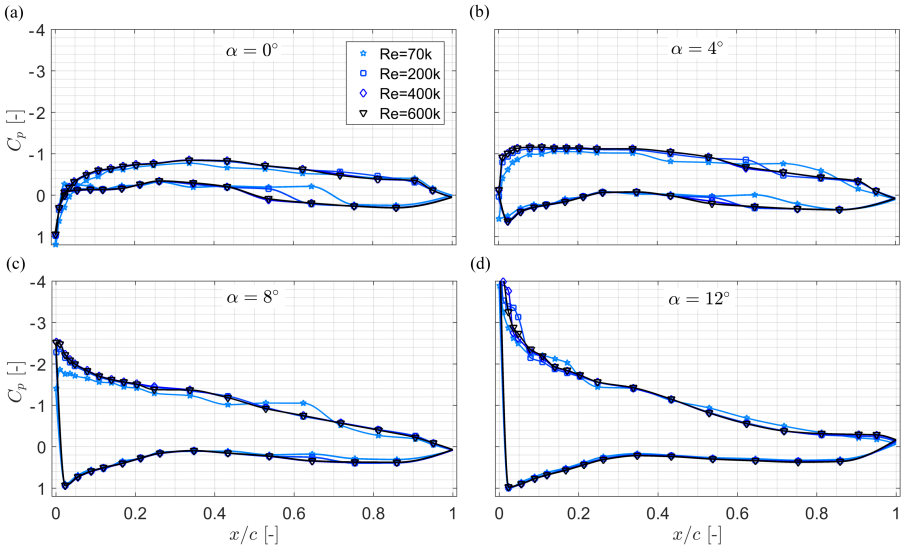

Figure 5: Comparison of mid-span surface pressure at **(a)** $\alpha = 0°$ **(b)** $\alpha = 4°$ **(c)** $\alpha = 8°$ and **(d)** $\alpha = 12°$ for $Re_c = 0.7 \times 10^5$, $Re_c = 2.0 \times 10^5$, $Re_c = 4.0 \times 10^5$ and $Re_c = 6.0 \times 10^5$.

pressure distributions generally match very well. Smaller separation bubbles are still observed for $Re = 2.0 \times 10^5$ at α=0° and α=4°.

4.2. Model predictions

In this section, the model predictions are compared to the experimental results at Re=1.0×10^5. In Figure 6 the model predictions at $\alpha = 2°, 4°, 8°, 10°$ and 12° are compared to the experimental lift and drag results. In addition to the results obtained from direct force measurements and wake momentum loss integration, lift and drag were calculated from surface pressure measured around the airfoil circumference at mid span. The lift characteristics from surface pressure thus give an indication about the local flow conditions at mid span and indicate the significant three-dimensional flow effects occurring at stall. A lower stall angle of about $\alpha \approx 10°$ and $C_{L,max}$ location are detected at mid-span. This can be explained by a significantly earlier flow separation at mid-span at the onset of stall. These three-dimensional flow effects are further investigated

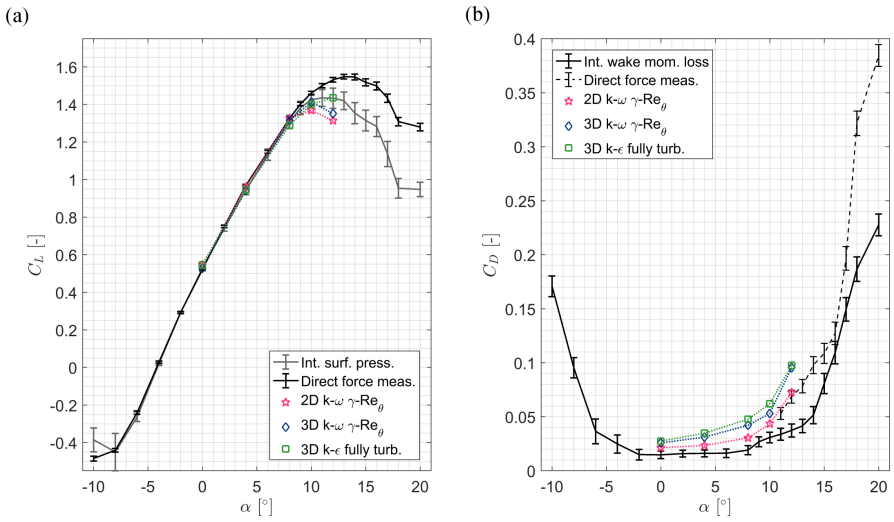

Figure 6: Comparison of **(a)** Lift and **(b)** drag coefficients at $Re = 1.0 \times 10^5$.

in the following section. In order to help evaluate the two-dimensionality of the experimental setup the $\gamma - Re_\theta$ is used for a 2D computational domain as well as a full 3D discretization of the model setup. As shown in Figure 6 (a) all three models utilized predict the lift coefficient in the linear region between $\alpha = 0 - 8°$ quite accurately. At the onset of stall at $\alpha = 12°$, however, the model predictions show a significant spread and the 2D $\gamma - Re_\theta$ model predicts a slightly lower value than the corresponding 3D simulation. Although it is incapable of predicting such transitional effects as laminar separation bubbles, the lift level predicted by the Realizable k-ϵ model's coincidentally matches the experimental results closer compared to the other two models at $\alpha = 12°$. Due to their considerably lower magnitude, the drag coefficients are more sensitive to quantify. The predictions by all three models are observed to slightly over-predict compared to the total drag measured by the momentum loss in the wake at mid span. The deviations for $\alpha = 0, 4$ and $8°$ are acceptably small, while the mismatch at $\alpha = 12°$ is considerably larger giving values almost twice as high as the experimental value. Almost no influence of the modeling of transitional

effects compared to the fully turbulent boundary layer simulations is observed in the 3D simulations. The drag results of the 2D model are seen to give slightly lower values than the corresponding 3D simulations.

A closer analysis of the pressure distributions reveals further details of the simulations as presented in Figure 7. Herein, the pressure coefficient C_P is compared for all four investigated angles of attack. The vertical bars given with the experimental curves are quantifying the standard deviation of the measured pressure fluctuations at mid-span. The experimental pressure distribution at $\alpha = 0°$ indicates local separation bubbles both at the pressure and suction side. Note that the localization of a laminar separation bubble is in most cases only based on a local variation in a single pressure tap. This only allows for a rough estimation of a laminar separation bubble, due to a limited resolution of pressure taps on both the pressure and suction surface. While the pressure side bubble occurs around $x/c = 0.5 - 0.6$, the suction side bubble is located closer to the trailing edge at $x/c = 0.8 - 0.9$. With increasing angle off attack the suction side bubble is observed to move upstream. At $\alpha = 12°$ it is located very close to the leading edge around $x/c = 0.05 - 0.10$ causing a significant jump in suction side pressure. For angles of attack $\alpha > 16°$ transition is observed to occur directly at the leading edge with the flow not being able to re-attach (not shown in graph). On the pressure side the separation bubble moves further downstream at increasing angle of attack and is eventually disappearing around $\alpha \geq 6°$. The surface pressure prediction by the $\gamma - Re_\theta$ model is observed to be comparable to the experimental results for $\alpha = 0 - 8°$, both in the 2D and 3D setup. The resulting surface pressure magnitudes and locations of the separation bubble are well predicted. The 2D and 3D simulations results are more or less congruent. At the onset of stall at $\alpha = 12°$, however, the suction side pressure predictions are observed to be considerably differing from the experimental values. Although the location of the separation bubble matches well with the experimental location, the suction side pressure level is predicted too high for a significant portion of the chord from $x/c = 0 - 0.60$. This also causes the separation point to move upstream in the $k - \omega$ simulation relative

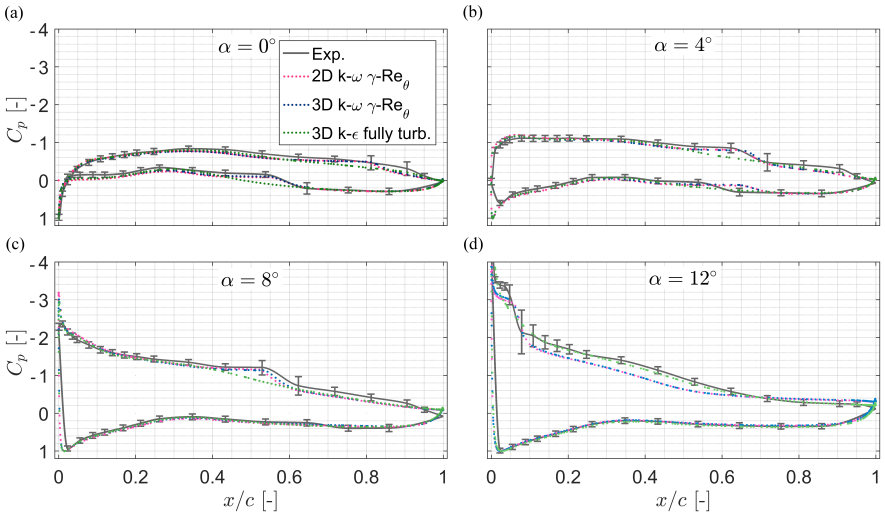

Figure 7: Comparison of mid-span surface pressure at **(a)** $\alpha = 0°$ **(b)** $\alpha = 4°$ **(c)** $\alpha = 8°$ and **(d)** $\alpha = 12°$ for $Re_c = 1.0 \times 10^5$.

to the k-ϵ simulation, and might be the main reason for the aforementioned under prediction in lift coefficient $C_{L,12°}$ at the same angle. Considering the relatively close agreement between the fully turbulent k-ϵ and the transitional $k-\omega$ simulations for $\alpha = 0-8°$ the effect of the LSB's on the lift and drag values are observed to be small in this range. At $\alpha = 12°$ the experimentally measured suction side pressure level is well matched by the Realizable k-ϵ model in contrast to the predictions by the $\gamma - Re_\theta$ model after the boundary layer transitions. As a consequence the lift coefficient computed by the k-ϵ simulation gives a closer approximation of the experimental value. A visualization of the turbulent kinetic energy (TKE) and mean velocity distributions around the airfoil simulated with the $3D\,\gamma - Re_\theta$ model at $Re_c = 1.0 \times 10^5$ is presented in Figure 8. At $\alpha = 8°$ and $\alpha = 12°$ the presence of laminar separation bubbles on the suction side is clearly observed. These are indicated by a local mean velocity drop and re-increase further downstream. The turbulent kinetic energy is observed to reach local maxima around the location of re-attachment. These locations corresponds well with the maximum pressure fluctuations measured

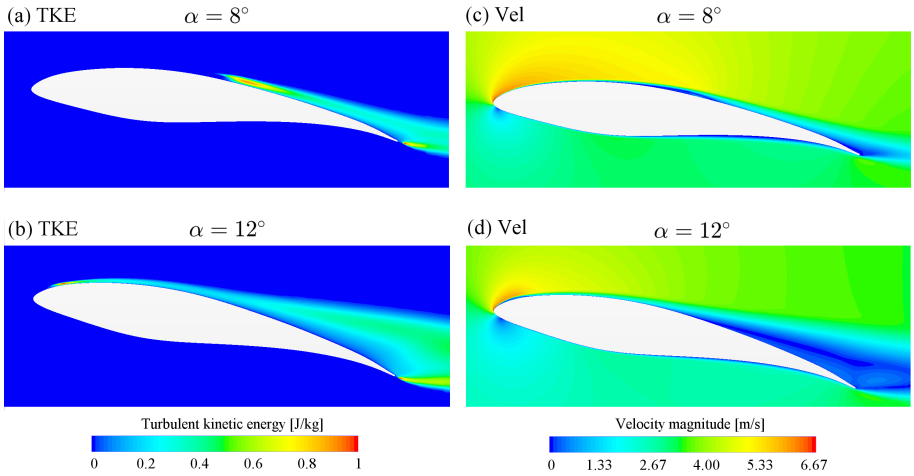

Figure 8: $3D\,\gamma - Re_\theta$ simulations at the mid-section symmetry plane at $Re_c = 1.0 \times 10^5$. **(a)** and **(b)** show the turbulent kinetic energy around the airfoil at $\alpha = 8°$ and $\alpha = 12°$ respectively. **(c)** and **(d)** show the corresponding velocity magnitude distributions at $\alpha = 8°$ and $\alpha = 12°$ respectively.

near the reattachment location of the LBS as previously shown in Figure 7. At $\alpha = 8°$ the LSB originates at $x/c \approx 0.4$ and extends almost 0.2 chord-lengths downstream, while it originates right after the leading edge for $\alpha = 12°$ and only measures about half the size. The TKE plots in Figure 8 (a) and (b) clearly show that the flow manages to re-attach in both cases. The flow is observed to fully separate around $x/c \approx 0.9$ for $\alpha = 8°$ and at $x/c \approx 0.5$ for $\alpha = 12°$. The boundary layer on the pressure side is observed to remain laminar for both angles of attack.

4.3. Sensitivity to inflow turbulence level

In order to quantify effects of inflow turbulence an additional computational sensitivity study was conducted at $Re = 1.0 \times 10^5$. Table 5 shows the results for lift and drag coefficients for three angles of attack $\alpha = 8$, 10 and 12° at three different inlet turbulence intensities $TI_{2\cdot c} = 0.71$, 0.56 and 0.22%. The investigated angles are chosen to be around the airfoil's stall point. The differ-

Table 5: Lift and drag coefficients at $Re = 1.0 \times 10^5$ as a function of different inlet turbulence intensities computed by 2D simulations with the $\gamma - Re_\theta$ model. The turbulent length scale was set according to Table 1.

		$\alpha = 8$ °		$\alpha = 10$ °		$\alpha = 12$ °	
TI_{inlet} [%]	$TI_{2\cdot c}$ [%]	C_L	C_D	C_L	C_D	C_L	C_D
0.94	0.71	1.330	0.02990	1.378	0.04305	1.324	0.07161
0.71	0.56	1.325	0.03049	1.370	0.04361	1.314	0.07263
0.25	0.22	1.309	0.03334	1.355	0.04525	1.277	0.07685
Standard deviation σ		0.01097	0.00184	0.01167	0.00114	0.02476	0.00277

ent inflow turbulence intensity levels are observed to significantly influence the resultant lift and drag coefficients. When decreasing the inflow turbulence considerably smaller lift and larger drag coefficients were simulated. As indicated by the computed standard deviation σ in the last row of Table 5, the variations in lift related to inflow turbulence increase with increasing angle of attack. Note that for the lowest inflow turbulence level the simulation for $\alpha = 12°$ displayed oscillatory convergence with normalized residuals in the order of 10^{-3}, possibly indicating that a proper steady state solution does not exist, and an accurate result may require a transient analysis.

4.4. Three-dimensional flow effects

As shown in Figure 6 (a) the lift coefficient results obtained from direct force measurements differ significantly from those obtained from mid-span surface pressure integration. This indicates that the local flow conditions at mid-span cannot be assumed to be representative for all span-wise wing cross sections, and the flow can no longer accurately be described as two-dimensional. On the contrary, considerable three-dimensional flow effects are observed as soon as the flow separates from the suction side surface. The surface flow of the non-stalled, partly-stalled and fully-stalled wing section is compared in Figure 9. For this purpose tufts of a length of $2.5cm$ have been taped to the suction

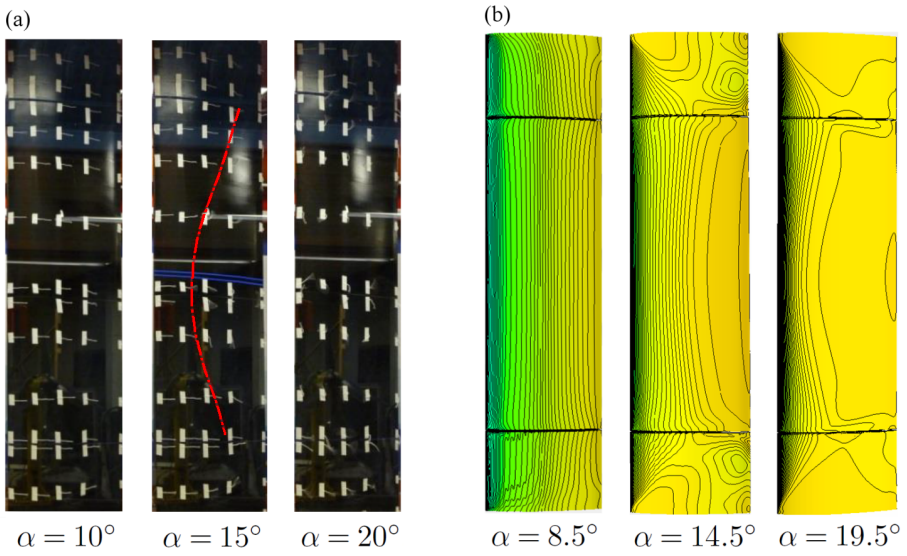

Figure 9: **(a)** Flow visualization on the suction side surface with tufts in the experiment. The red line approximates the locations of flow separation. The blue lines indicate the location of the mid-span pressure taps. **(b)** Iso-lines of constant pressure on the suction side surface from the 3D k-ϵ fully turbulent simulation.

side of the wing in the experiment, while iso-line of constant surface pressure are extracted from the $3D$ Realizable $k-\epsilon$ simulation. This allows only a very qualitative comparison, but the three-dimensionality of the flow becomes apparent at $\alpha = 15°$ both in the experiment and the simulation. While the flow is still fairly attached at $\alpha = 8-10°$ as indicated by aligned tufts in the experiment and parallel isobars in the simulation, the surface flow clearly separates for $\alpha = 14-15°$. A big part of the tufts are observed to begin fluttering. At the wing's mid-span the separation is seen to happen in the first half of the wing's chord. With increasing distance from the mid-section the flow separation is observed to occur further downstream, which is indicated by the approximated red line. The 3D simulation supports this observation by the means of surface pressure isobars. At the partly-stalled $\alpha = 15°$ significant 3D flow establishes indicating a faster pressure increase at mid-span than further from the center. A

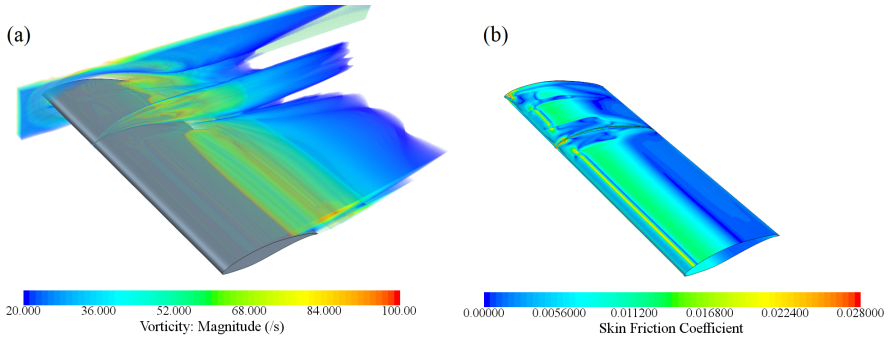

Figure 10: Visualizations of 3D flow for $\alpha = 12°$: **(a)** A volume render of vorticity. **(b)** Skin friction coefficient.

complex flow is simulated on the wing dummy sections close to the wall boundary layers of the wind tunnel domain. The gap between the wing's main section and the dummies was assessed not to have a significant qualitative influence on the flow structures [12] although vortex shedding is predicted as is illustrated in Figure 10 (a). The earlier separation at the wing's mid-section is assumed to be an effect of so-called stall cell vortices, which is assumed to interact with the separation line vortex as described in [18]. At $\alpha = 19 - 20°$ the complete wing section is fully-stalled. While the gap separating the wing wall dummies and the main section may not have a significant effect on the pressure distribution and lift coefficient, increased skin-friction clearly affects the drag as shown in Figure 10 (a). This is clearly observed in a comparison of lift and drag values of cases A and C in Table 6. Case A is a digital copy of the split wing model with its 2 mm gaps, while case C represents a virtually split wing with no physical gaps at all. In general, a relatively small impact on the computed lift coefficients of less than 0.8% is observed. Moreover, the lift and drag coefficients for a wall-to-wall measurement are included (case B). As expected, the lift coefficients are consistently lower when including the wall boundary layers, especially for higher angles of attack. Comparing cases B and C, a difference in lift coefficients of about 6.5% is observed, indicating that the complex near-wall flow structures

Table 6: Results from 3D simulations with the Realizable $k-\epsilon$ turbulence model. Lift and drag coefficients were computed in three different ways: A - summation of surface forces on the main wing section (without dummy sections); B - summation of surface forces wall-to-wall for a split blade geometry (including dummy sections); C - summation of surface forces on a virtual central measuring section computed on a continuous blade geometry (no splits).

	$\alpha = 4\ ^\circ$		$\alpha = 10\ ^\circ$		$\alpha = 12\ ^\circ$	
case	C_L	C_D	C_L	C_D	C_L	C_D
A	0.948	0.0350	1.370	0.0694	1.436	0.0976
B	0.926	0.0349	1.296	0.0737	1.308	0.1062
C	0.958	0.0308	1.396	0.0574	1.424	0.0903

would significantly influence the force coefficients for a wall-to-wall setup. Noticeably, also the computed drag coefficients are roughly 10-25% lower in case C, as secondary flows from the gaps and drag inducing wall effects are not taken into account in this case. This quantification largely explains the excessive values obtained for the drag coefficient from the 3D simulations, relative to the measured values at mid-span and the 2D simulation results.

5. Discussion

The presented experimental lift and drag results show a relatively stable performance for all assessed Reynolds numbers of $Re \geq 0.7 \times 10^5$. At the lowest measured Reynolds number $Re = 0.5 \times 10^5$, transitional effects are observed to significantly influence the airfoil's performance. In contrast to that, measurements by Sarmast and Mikkelsen [7] at DTU found a clear Reynolds number dependent performance for $Re \leq 0.8 \times 10^5$. These differences are considered to stem from the considerably lower turbulence level of $TI_{DTU} < 0.2\%$ at such low Reynolds numbers in DTU's facilities compared to what is achieved in NTNU's ($TI_{NTNU,Re=70k} = 0.7\%$) wind tunnel. The key geometry and turbulence parameters of three different experimental measurement campaigns at different institutions are compared in Table 7. As can be observed in Figure 11 the

experimental results of the lift coefficient match well with earlier experiments presented by Sarlak et al. [8] and Ostovan et al. [9] up to $\alpha \approx 6°$. However, significant differences are found for the stall angle and peak lift location. METU's measurements indicate the onset of stall already around $\alpha = 6 - 7°$, while reaching a maximum lift of $C_{L,max,METU} = 1.2$ and remaining at that level until α=16°. The reasons for these strong differences in an earlier onset of stall and significantly smaller peak lift are not straight forward to explain. The inlet turbulence level is similar in METU's and NTNU's experiment, while the different stall behaviour might be due to different wing geometries. Aside from the dummies used in NTNU's experiment, which cancel out lift-decreasing separation effects near at the wing ends, the geometries also feature different aspect ratios. This might influence the characteristics of the three-dimensional flow at the onset of stall. As shown by Manolesos et al. (2014), the wing's AR influences the relative stall cell (SC) area. For lower ARs the relative SC area was observed to be higher. The model used METU had an aspect ratio $AR_{DTU} = AR_{METU} = 5.0$, while NTNU's setup features a smaller ratio of about $AR_{NTNU} \approx 4.0$. In the case of DTU's measurements flow separation on the suction side flow begins around α=9°, slightly earlier as in the present NTNU measurements, but is much more abrupt. A significantly lower peak lift coefficient of $C_{L,max,DTU} = 1.35$ is measured, which is observed to increase for higher Reynolds numbers [7]. The considerably lower inflow turbulence level in DTU's experiments could explain the sudden drop in lift, compared to NTNU's

Table 7: Comparison of geometrical dimensions and inflow turbulence levels for different experimental measurement campaigns on the NREL S826 profile.

Exp. campaign	chord L_C [m]	span [m]	AR [-]	$TI_{Re=100k}$ [%]
NTNU	0.45	1.78	4.0	0.70
DTU	0.10	0.50	5.0	0.20
METU	0.20	1.00	5.0	0.60

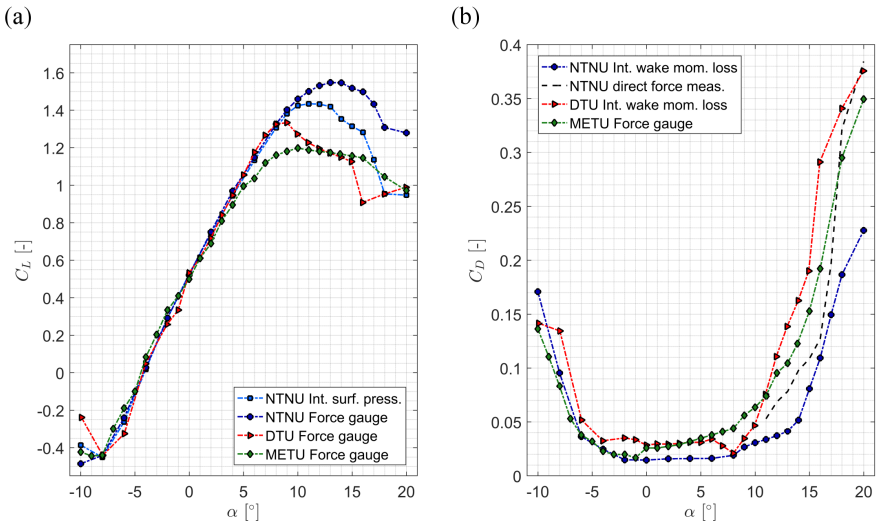

Figure 11: Comparison of the lift and drag coefficients of three different experimental datasets measured at NTNU, DTU and METU at $Re = 1.0 \times 10^5$.

results measured at an about three times higher inflow turbulence intensity. As previously seen in Figure 8 the LSB for α=8° is positioned on the ridge of the suction side of the airfoil, and moves gradually upstream as the angle of attack is increased. If the turbulent mixing is not high enough to sufficiently energize the boundary layer, the flow will not re-attach and an abrupt stall could occur. The variation in different drag coefficient results is large, also for attached flow conditions. Although a comparable drag coefficient of $C_{D,min,METU} = 0.017$ is measured at α=-1° in METU's experiments, the drag seems to jump to a much higher level for $\alpha = 0 - 6°$, relative to the present measurements. The opposite trend is observed in DTU's drag results, where the minimum drag of $C_{D,min,DTU} = 0.021$ is measured at α=8° right before stall occurs. However, the drag level is considerably higher from $\alpha = -4° - 7°$, which is in accordance with separated flow and the abrupt loss in generation of lift. In comparision the NTNU results from wake momentum loss integration show a consistently low drag coefficient of $C_{D,NTNU} = 0.015 - 0.016$ from $\alpha = -2° - 6°$. As reflected in the gradual decrease in the measured lift, flow separation at the onset of

stall seem to be much more docile in the present measurements. The drag first increases only slightly around $\alpha = 9°$ before rising strongly around $\alpha = 15°$. Note however that due to three-dimensional effects, the wake momentum deficit measured at mid span is not expected to give accurate results for the drag-coefficient beyond an angle of attack of $\alpha = 10°$.

Comparison with previous numerical simulations performed on the S826 airfoil seem to confirm a higher maximum lift coefficient relative to previous measurements in the present Reynolds number range, although the numerical prediction of stalled flow is still observed to be difficult. LES computations by Sarlak et al. [8] resulted in a maximum lift of $C_{L,max,DTU,LES} = 1.54$ at $\alpha = 12°$ ($Re = 1.0 \times 10^5$). Also, computations by Cakmakcioglu et al. [14] at the same Reynolds number indicate a significantly higher lift coefficient level than in METU's experiments. In a Delayed Detached Eddy Simulation (DDES) they find a maximum lift coefficient of $C_{L,max,METU,DDES} = 1.38$ and their $2D$ realizable $k-\epsilon$ model results in a lift of $C_{L,max,METU,k-\epsilon} = 1.44$, both computed at $\alpha = 10°$.

6. Conclusions

A combined experimental and numerical study on a wing section of the NREL S826 airfoil at low to moderate Reynolds numbers was realized. The lift and drag characteristics is observed to be strongly affected by transitional effects for Reynolds numbers lower than $Re < 0.7 \times 10^5$. Also, at larger Reynolds numbers, smaller laminar separation bubbles are seen to appear on the airfoil's pressure and suction side. Lift characteristics at the wing's mid-span position significantly differ from force measurements on the entire wing, which is in accordance with strong three-dimensional flow effects observed at the onset of stall.

A computation of the test case with the transitional $\gamma - Re_\theta$ model by Langtry-Menter was able to accurately predict the location and the resulting mean sur-

face pressure variations of laminar separation bubbles. In partly stalled flow conditions both turbulence models showed a tendency to under-predict the generated lift. Furthermore, the effects of two- versus three-dimensional computational domains was investigated showing differences at the onset of stall. Deviations in computed and measured drag coefficients are observed at the onset of stall, motivating a drag calculation at mid-span for more accurate future comparisons.

A comparison to earlier experiments realized on the same airfoil at DTU and METU showed a good agreement in the linear lift region. Significant differences are observed at the stall angle and maximum lift, with the presented NTNU data resulting in considerably higher maximum lift. The present combined experimental and numerical investigation suggests that these discrepancies in the stall region can be largely explained by the difference in free stream turbulence and aspect ratio of the geometrical setup.

Acknowledgements. The authors would like to acknowledge Nikolai Yde Aksnes for the great effort in designing the wing and conducting the first set of experiments. Arnt Egil Kolstad is acknowledged for the assistance in design and assembling of the wing model. Thomas H. Hansen is acknowledged for his initial ideas and input to the design of this project. SIEMENS is acknowledged for providing an academic license and support for StarCCM+. This research was supported with computational resources at NTNU provided by NOTUR.

References

[1] J. N. Sørensen, General Momentum Theory for Horizontal Axis Wind Turbines, 1st Edition, Vol. 4 of Research Topics in Wind Energy, Springer International Publishing Switzerland, 2016. doi:10.1007/978-3-319-22114-4.

[2] D. M. Somers, The s825 and s826 airfoils, Tech. Rep. SR-500-36344, NREL (2005).

URL https://wind.nrel.gov/airfoils/Documents/S825,S826_Design.pdf

[3] P.-Å. Krogstad, P. Eriksen, Blind test calculations of the performance and wake development for a model wind turbine, Renewable Energy 50 (2012) 325–333. doi:10.1016/j.renene.2012.06.044.

[4] F. Pierella, P.-Å. Krogstad, L. Sætran, Blind test 2 calculations for two in-line model wind turbines where the downstream turbine operates at various rotational speeds, Renewable Energy 70 (2014) 62–77. doi:10.1016/j.renene.2014.03.034.

[5] P.-Å. Krogstad, L. Sætran, M. Adaramola, Blind test 3 calculations of the performance and wake development behind two in-line and offset model wind turbines, Journal of Fluids and Structures 52 (2014) 65 – 80. doi:10.1016/j.jfluidstructs.2014.10.002.

[6] J. Bartl, L. Sætran, Blind test comparison of the performance and wake flow between two in-line wind turbines exposed to different turbulent inflow conditions, Wind Energy Science 2 (1) (2017) 55–76. doi:10.5194/wes-2-55-2017.

[7] S. Sarmast, R. Mikkelsen, The experimental results of the nrel s826 airfoil at low reynolds numbers, Tech. rep., KTH (2013).
URL urn:nbn:se:kth:diva-120583

[8] H. Sarlak, R. Mikkelsen, S. Sarmast, J. N. Sørensen, Aerodynamic behaviour of nrel s826 airfoil at re=100 000, J. Phys.: Conf. Series 524 (2014) 012027. doi:10.1088/1742-6596/524/1/012027.

[9] Y. Ostovan, H. Amiri, O. Uzol, Aerodynamic characterization of nrel s826 airfoil at low reynolds numbers, in: Conference on Wind Energy Science and Technology-RUZGEM, 2013.

[10] M. O'Meara, T. Mueller, Laminar separation bubble characteristics on an airfoil at low reynolds numbers, AIAA Journal 25 (1987) 1033–1041. doi:10.2514/3.9739.

[11] M. F. Kerho, M. B. Bragg, Airfoil boundary-layer development and transition with large leading-edge roughness, AIAA Journal 35 (1997) 75–84. doi:10.2514/2.65.

[12] K. Sagmo, J. Bartl, L. Sætran, Numerical simulations of the nrel s826 airfoil, Journal of Physics: Conference Series 753 (2016) 082036. doi:10.1088/1742-6596/753/8/082036.

[13] R. B. Langtry, F. R. Menter, Correlation-based transition modeling for unstructured parallelized computational fluid dynamics codes, AIAA Journal 47 (12) (2009) 2894–2906. doi:10.2514/1.42362.

[14] S. C. Cakmakcioglu, I. O. Sert, O. Tugluk, N. Sezer-Uzol, 2-d and 3-d cfd investigation of nrel s826 airfoil at low reynolds numbers, J. Phys.: Conf. Series 524 (2014) 012028. doi:10.1088/1742-6596/524/1/012028.

[15] H. Sarlak, Large eddy simulation of turbulent flows in wind energy, Ph.D. thesis, DTU Wind Energy (2014).

[16] A. E. Winkelmann, J. B. Barlow, Flowfield model for a rectangular planform wing beyond stall, AIAA Journal 18 (8) (1980) 1006–1008. doi:10.2514/3.50846.

[17] D. Weihs, J. Katz, Cellular patterns in poststall flow over unswept wings, AIAA Journal 21 (12) (1983) 1757–1759. doi:10.2514/3.8321.

[18] M. Manolesos, G. Papadakis, S. Voutsinas, Experimental and computational analysis of stall cells on rectangular wings, Wind Energy 17 (2014) 939–955. doi:10.1002/we.1609.

[19] M. Manolesos, S. Voutsinas, Geometrical characterization of stall cells on rectangular wings, Wind Energy 17 (2014) 1301–1314. doi:10.1002/we.1634.

[20] M. Schultz, K. Flack, The rough-wall turbulent boundary layer from the hydraulically smooth to the fully rough regime, Journal of Fluid Mechanics 580 (2007) 381–405. doi:10.1017/S0022112007005502.

[21] J. Barlow, W. Rae, A. Pope, Low-Speed Wind Tunnel Testing, 3rd Edition, Wiley, 1999.

[22] A. Wheeler, A. Ganji, Introduction to Engineering Experimentation, 3rd Edition, Pearson Education, 2004.

[23] P. Malan, K. Suluksna, E. Juntasaro, Calibrating the $\gamma - re_\theta$ transistion model for commercial cfd, in: the 47th AIAA Aerospaces Sciences Meeting, 2009. doi:10.2514/6.2009-1142.

[24] M. Wolfshtein, The velocity and temperature distribution in one-dimensional flow with turbulence augmentation and pressure gradient, International Journal of Heat and Mass Transfer 12 (1969) 301–318. doi:10.1016/0017-9310(69)90012-X.

[25] CD-adapco, StarCCM+ user guide, code version 10.02.012.

[26] R. B. Langtry, A correlation-based transition model using local variables for unstructured parallelized cfd codes, Ph.D. thesis, University of Stuttgart (May 2006).

[27] H. K. Versteeg, W. Malalasekera, An Introduction to Computational Fluid Dynamics, 2nd Edition, Pearson Education, Harlow, 2007.

[28] I. B. Celik, U. Ghia, P. J. Roache, C. Freitas, H. Coleman, P. E. Raad, Procedure for estimation and reporting of uncertainty due to discretization in cfd applications, Journal of Fluids Engineering; Transactions of the ASME 130 (078001). doi:10.1115/1.2960953.

[29] P. Roache, Quantification of uncertainty in computational fluid dynamics, Annu. Rev. Fluid. Mech. 29 (1997) 123–60. doi:10.1146/annurev.fluid.29.1.123.

Appendix: Experimental lift and drag data

The lift coefficients C_L and drag coefficients C_D for all measured Reynolds numbers are listed in Tables 8 and 9 respectively. The tabulated profile coordinates of marginally modified NREL S826 profile and all data for the presented pressure coefficients C_P are available on request to the corresponding author.

Table 8: Lift coefficients obtained from direct force measurements at the main section of the wing for all investigated Reynolds numbers.

	$Re =$	$Re =$	$Re =$	$Re =$	$Re =$	$Re =$	$Re =$	$Re =$
α [°]	$50k$	$70k$	$100k$	$200k$	$300k$	$400k$	$500k$	$600k$
-15	-0.4443	-0.4557	-0.4538	-0.4420	-0.4268	-0.4116	-0.4038	-0.4021
-10	-0.4815	-0.4828	-0.4851	-0.4929	-0.4747	-0.4545	-0.4423	-0.4313
-8	-0.4011	-0.4451	-0.4408	-0.3871	-0.3429	-0.2941	-0.2745	-0.2630
-6	-0.2992	-0.2761	-0.2399	-0.1397	-0.0761	-0.0698	-0.0640	-0.0704
-4	-0.0964	-0.0009	0.0275	0.1287	0.1595	0.1640	0.1611	0.1549
-2	0.1998	0.2423	0.2926	0.3632	0.3828	0.3857	0.3782	0.3734
0	0.4585	0.4839	0.5217	0.5758	0.5944	0.6003	0.5969	0.5921
2	0.5923	0.7285	0.7506	0.7866	0.8054	0.8154	0.8141	0.8127
4	0.7357	0.9512	0.9695	0.9948	1.0144	1.0269	1.0283	1.0293
6	0.8719	1.1165	1.1478	1.1782	1.1999	1.2161	1.2185	1.2206
8	1.2814	1.3052	1.3265	1.3483	1.3594	1.3655	1.3628	1.3648
9	1.4124	1.3836	1.4028	1.4156	1.4159	1.4202	1.4205	1.4260
10	1.4290	1.4489	1.4607	1.4636	1.4655	1.4747	1.4782	1.4846
11	1.4057	1.4956	1.5005	1.5045	1.5103	1.5189	1.5243	1.5348
12	1.3637	1.5287	1.5318	1.5315	1.5359	1.5480	1.5558	1.5709
13	1.3273	1.5483	1.5483	1.5380	1.5410	1.5554	1.5635	1.5813
14	1.2984	1.5533	1.5467	1.5277	1.5306	1.5458	1.5526	1.5778
15	1.1323	1.5178	1.5179	1.5113	1.5101	1.5174	1.5226	1.5513
16	0.9309	1.4925	1.4989	1.4955	1.4907	1.4874	1.4834	1.5032
17	0.9572	1.4246	1.4333	1.4081	1.4028	1.4470	1.4429	1.4516
18	0.9893	1.2977	1.3085	1.2798	1.2658	1.3584	1.3743	1.4007
20	1.0653	1.2951	1.2793	1.2372	1.1867	1.1655	1.2011	1.2674
25	1.1090	1.1947	1.1870	1.1850	1.1627	1.1435	1.1307	1.1271
30	1.2318	1.2560	1.2224	1.1791	1.1685	1.1768	1.1794	1.1708

Table 9: Drag coefficients obtained from momentum loss calculations in the wake at midspan for all investigated Reynolds numbers.

α [°]	$Re = 50k$	$Re = 70k$	$Re = 100k$	$Re = 200k$	$Re = 300k$	$Re = 400k$	$Re = 500k$	$Re = 600k$
-15	0.2896	0.2761	0.2510	0.2401	0.2333	0.2219	0.2104	0.2089
-10	0.2324	0.2148	0.1709	0.1415	0.1568	0.1382	0.1414	0.1444
-8	0.1909	0.1673	0.0954	0.0546	0.0691	0.0571	0.0567	0.0547
-6	0.0614	0.0581	0.0365	0.0363	0.0252	0.0208	0.0197	0.0183
-4	0.0335	0.0367	0.0248	0.0216	0.0149	0.0145	0.0124	0.0118
-2	0.0271	0.0286	0.0149	0.0160	0.0131	0.0112	0.0102	0.0096
0	0.0242	0.0243	0.0147	0.0128	0.0125	0.0112	0.0105	0.0094
2	0.0344	0.0255	0.0159	0.0163	0.0128	0.0128	0.0116	0.0104
4	0.0456	0.0263	0.0161	0.0169	0.0140	0.0133	0.0124	0.0116
6	0.0632	0.0276	0.0162	0.0183	0.0159	0.0140	0.0136	0.0130
8	0.0589	0.0283	0.0191	0.0197	0.0180	0.0175	0.0170	0.0173
9	0.0450	0.0299	0.0268	0.0228	0.0217	0.0219	0.0212	0.0205
10	0.0547	0.0352	0.0308	0.0275	0.0260	0.0256	0.0247	0.0237
11	0.0624	0.0405	0.0338	0.0305	0.0308	0.0298	0.0290	0.0290
12	0.0753	0.0448	0.0374	0.0358	0.0355	0.0363	0.0351	0.0354
13	0.0934	0.0484	0.0415	0.0432	0.0380	0.0423	0.0423	0.0410
14	0.1095	0.0615	0.0517	0.0569	0.0434	0.0467	0.0473	0.0458
15	0.1384	0.0896	0.0809	0.0749	0.0669	0.0631	0.0632	0.0610
16	0.1799	0.1198	0.1095	0.1015	0.1035	0.1035	0.1067	0.1054
17	0.2156	0.1697	0.1495	0.1418	0.1341	0.1333	0.1453	0.1530
18	0.2469	0.1988	0.1867	0.1757	0.1645	0.1587	0.1871	0.1933
20	0.2892	0.2389	0.2277	0.2273	0.2150	0.2058	0.2295	0.2258
25	0.3244	0.3210	0.3133	0.3132	0.3151	0.3069	0.3067	0.3052
30	0.3555	0.3486	0.3392	0.3372	0.3323	0.3251	0.3352	0.3349